Dalton
Transactions

Cite this: *Dalton Trans.*, 2012, **41**, 6232

www.rsc.org/dalton

PAPER

SMARTER crystallography of the fluorinated inorganic–organic compound $Zn_3Al_2F_{12}\cdot[HAmTAZ]_6$†

Charlotte Martineau,*[a] Amandine Cadiau,‡[b] Boris Bouchevreau,[a] Jürgen Senker,[c] Francis Taulelle[a] and Karim Adil*[b]

Received 15th January 2012, Accepted 16th March 2012
DOI: 10.1039/c2dt30100h

We present in this paper the structure resolution of a fluorinated inorganic–organic compound—$Zn_3Al_2F_{12}\cdot[HAmTAZ]_6$—by SMARTER crystallography, *i.e.* by combining powder X-ray diffraction crystallography, NMR crystallography and chemical modelling of crystal (structure optimization and NMR parameter calculations). Such an approach is of particular interest for this class of fluorinated inorganic–organic compound materials since all the atoms have NMR accessible isotopes (^{1}H, ^{13}C, ^{15}N, ^{19}F, ^{27}Al, ^{67}Zn). In $Zn_3Al_2F_{12}\cdot[HAmTAZ]_6$, ^{27}Al and high-field ^{19}F and ^{67}Zn NMR give access to the inorganic framework while ^{1}H, ^{13}C and ^{15}N NMR yield insights into the organic linkers. From these NMR experiments, parts of the integrant unit are determined and used as input data for the search of a structural model from the powder diffraction data. The optimization of the atomic positions and the calculations of NMR parameters (^{27}Al and ^{67}Zn quadrupolar parameters and ^{19}F, ^{1}H, ^{13}C and ^{15}N isotropic chemical shifts) are then performed using a density functional theory (DFT) based code. The good agreement between experimental and DFT-calculated NMR parameters validates the proposed optimized structure. The example of $Zn_3Al_2F_{12}\cdot[HAmTAZ]_6$ shows that structural models can be obtained in fluorinated hybrids by SMARTER crystallography on a polycrystalline powder with an accuracy similar to those obtained from single-crystal X-ray diffraction data.

1. Introduction

Although both diffraction equipment and computing methods have greatly improved over the past decade, *ab initio* structure solution still remains highly challenging for powders,[1] in particular for compounds lacking long-range order. A novel approach combining diffraction with high-resolution solid-state nuclear magnetic resonance (NMR) and quantum mechanical calculations has recently emerged as an efficient way to overcome the intrinsic difficulties of powders. This so-called SMARTER crystallography (structure elucidation by combining magnetic resonance, computational modeling and diffractions) encompasses many structural analyses using the combination of such methods. It takes advantage of NMR atom resolved spectroscopy with a more local character to assist, improve and perform structure determination together with powder diffraction. The information extracted from solid-state NMR data can be used at different stages of the structure resolution process, ranging from the determination or validation of a space group over building of a structural model up to the structure refinement. One (1D) and two-dimensional (2D) NMR spectra indeed reflect the number, nature and multiplicity of the crystallographically inequivalent atoms or block of atoms in the integrant unit (the integrant unit—IU—is the first multiple of the asymmetric unit that has integer crystallographic multiplicities for all atoms in the unit cell)[2] as well as their relative positions, and the combination of the measurement of NMR parameters (chemical shift, quadrupolar or scalar tensors…) with their *ab initio* calculations has been shown to improve the accuracy of the atomic coordinates initially determined from diffraction data. The use of NMR also allows getting insights in various sub-networks that are usually difficult to access from diffraction measurements, like ionic mobility, the localization of organic templates in organic–inorganic hybrid compounds, the distribution of iso-electronic atoms

---

[a] *Tectospin – Institut Lavoisier de Versailles, CNRS UMR 8180, Université de Versailles Saint-Quentin en Yvelines, 45 Avenue des États-Unis, 78035 Versailles Cedex, France. E-mail: charlotte.martineau@chimie.uvsq.fr; Tel: +33139254260*
[b] *LUNAM Université, Université du Maine, CNRS UMR 6283, Institut Moléculaire du Mans, Avenue Olivier Messiaen, 72085 Le Mans, Cedex 9, France. E-mail: karim.adil@univ-lemans.fr; Tel: +33243833352*
[c] *Anorganische Chemie III, Universität Bayreuth, Universitätsstr. 30, 95447 Bayreuth, Germany. E-mail: juergen.senker@uni-bayreuth.de; Tel: +49921552538*

† Electronic supplementary information (ESI) available: Conditions of X-ray data collection, experimental and calculated XRPD diagram, instruction and output files for the space group determination, differences between the fractional atomic positions of the DFT-optimized structure and of the model determined from single-crystal X-ray diffraction of $Zn_3Al_2F_{12}\cdot[HAmTAZ]_6$. CCDC reference number 871623. For ESI and crystallographic data in CIF or other electronic format see DOI: 10.1039/c2dt30100h

‡ Current address: CICECO, Complexo de Laboratórios Tecnológicos Campus Universitário de Santiago 3810-193, Aveiro, Portugal.

or group of atoms (Si/Al, F/OH…). SMARTER crystallography has provided structural models of a wide variety of material classes, ranging from small organic molecules[3–5] and pharmaceuticals[6–8] over semiconductors for optical applications,[9,10] inorganic fluorides,[11–15] to porous systems like zeolites,[16–21] or metal–organic-framework (MOFs),[22–29] which have been described with a high degree of accuracy.

Fluorinated hybrid materials, in particular, fluorinated metal–organic frameworks (F-MOFs), sometimes exhibit enhanced thermal stability, low surface tension and improved physico-chemical performances compared to fully hydrogenated MOFs,[30–34] in particular in the presence of water.[35–38] However, to date, only a few materials built up from fluorinated inorganic frameworks have been reported in the literature.[39–41] Recently, we have shown that F-MOFs, resulting from the inclusion of aluminium with the possibility of generating cationic linkers by association of Zn^{2+} cations with triazolate molecules, could be obtained by hydrothermal synthesis.[42] In this paper, we present a new fluorinated hybrid compound obtained from hydrothermal synthesis with 3-aminotriazole (AmTAZ) organic linker, $Zn_3Al_2F_{12}\cdot[HAmTAZ]_6$.

The structure elucidation of this sample represents a case study for SMARTER crystallography since all atoms, both in the inorganic framework (^{27}Al, ^{67}Zn, ^{19}F) and the organic linkers (^{1}H, ^{13}C, ^{15}N) can be measured by solid-state magic angle-spinning (MAS) NMR. X-ray powder diffraction (XRPD) and high-resolution one-dimensional (1D) ^{13}C, ^{15}N, ^{1}H, ^{19}F, ^{67}Zn and ^{27}Al and 2D ^{1}H NMR data are used to select the space group and partially determine the integrant unit by identifying blocks of atoms as sub-units. Emphasis is given on NMR experimental issues (quantitative measurements, spectral resolution…) related to each nuclei probed in this study. The search for a structural model is then carried out by a Monte Carlo approach in direct space, using parts of the sub-integrant units as input data. The optimization of the atomic positions and the calculations of NMR parameters (^{27}Al and ^{67}Zn quadrupolar parameters and ^{19}F, ^{1}H, ^{13}C and ^{15}N isotropic chemical shifts) are done by *ab initio* quantum calculations. The structural model proposed for $Zn_3Al_2F_{12}\cdot[HAmTAZ]_6$ is validated and its accuracy assessed by comparing the experimental and DFT-calculated NMR parameters. An independent structural model was also obtained from single-crystal diffraction data. We show that the structural model provided for $Zn_3Al_2F_{12}\cdot[HAmTAZ]_6$ from powder diffraction data by SMARTER crystallography has an accuracy similar to that of single-crystal X-ray diffraction data, including the localization of the protons.

2. Experimental

2.1. Synthesis

$Zn_3Al_2F_{12}\cdot[HAmTAZ]_6$ has been synthesized from a mixture of ZnO (Merk), $Al(OH)_3$ (Merk), 3-amino-1,2,4-triazole (Aldrich), hydrofluoric acid solution (40% HF, Prolabo) and water. The hydrothermal reaction has been performed in a Parr Teflon® enclosure system at 160 °C by classical heating for 48 hours. The obtained solid polycrystalline powder has been washed with water and dried at room temperature. A single-crystal of sufficient size could be extracted from this powder.

2.2. Thermal analysis

Differential thermal analysis (DTA) and thermogravimetric analysis (TGA) curves of $Zn_3Al_2F_{12}\cdot[HAmTAZ]_6$ were recorded on a TA Instruments SDT-Q600 apparatus under argon, for temperatures up to 800 °C, with a 5 °C min^{-1} heating rate.

2.3. X-ray diffraction

The powder X-ray diffraction pattern of $Zn_3Al_2F_{12}\cdot[HAmTAZ]_6$ has been recorded at room temperature under air in a Bragg–Brentano geometry with a PANalytical MPD-PRO diffractometer using Cu K_α radiation in the 4–99° 2θ range and a 0.017° interpolated step. The Rietveld[43] method using the Fullprof[44] program was used for the structural refinement.

The single-crystal X-ray intensity data were collected on a Bruker APEX II Quazar diffractometer (4-circle Kappa goniometer, Iμs microfocus source, CCD detector) at 173 K. Empirical absorption corrections were applied. The structure solution was solved by direct methods (SHELXS-97),[45] extended by successive difference Fourier syntheses and refined by full-matrix least-square on all F^2 data using SHELXL-97; these programs are included in the WinGX[46] package. All non-hydrogen atoms were refined with anisotropic thermal parameters. All hydrogen atoms were generated and refined isotropically.

2.4. Solid-state NMR

The ^{27}Al single-pulse MAS (8 kHz) NMR spectrum of $Zn_3Al_2F_{12}\cdot[HAmTAZ]_6$ was recorded from powdered sample on an Avance 500 Bruker spectrometer (B_0 = 11.6 T, Larmor frequency = 130.3 MHz) using a 2.5 mm probe, a 1 μs pulse length, a recycle delay of 3 s and ^{19}F 64-step small-phase incremental alternation (SPINAL-64)[47] decoupling (radio-frequency field corresponding to a nutation frequency of 70 kHz). 256 transients were accumulated.

The ^{67}Zn static NMR spectrum was taken on an Avance 750 Bruker (Larmor frequency = 42.9 MHz) using a 4 mm probe. A Hahn-echo (inter-pulse delay of 100 μs) sequence was used, with 90° pulse length of 3.5 μs, and the full echo was recorded. The recycle delay was set to 0.5 s and ∼110 000 transients were accumulated (∼15 hours).

The ^{13}C NMR spectra were recorded on an Avance 500 Bruker (Larmor frequency = 125.8 MHz) using 3.2 and 4 mm probes. Cross-polarization polarization inversion (CPPI)[48] curves were recorded at a spinning frequency of 8 kHz, using CP[49] conditions that fulfill the $n = +1$ Hartmann–Hahn[50] condition (50 kHz RF pulse on ^{13}C) and 1 ms contact time. ^{13}C Hahn-echo spectra were recorded at a MAS frequency of 20 kHz using various inter-pulse delays synchronized with 1 to 4 rotor periods, 3.3 μs 90° pulse length, 400 s recycle delay and 160 transients for each spectrum. The ^{15}N cross-polarization (CP) MAS (5 kHz) NMR spectrum was recorded on an Avance II 300 Bruker spectrometer (B_0 = 7 T, Larmor frequency = 30.4 MHz) using a 7 mm probe. The CP transfer was done using 50 kHz RF on ^{1}H and fulfilling the $n = +1$ Hartmann–Hahn condition ($\nu_{nut}(^{15}N) = \nu_{nut}(^{1}H) - \nu_{rot}$). The contact time was set to 7 ms, the recycle delay to 15 s and ∼16 000 transients were accumulated. In all ^{13}C and ^{15}N NMR spectra, ^{1}H SPINAL-64 decoupling with a nutation frequency of 80 kHz was applied during the acquisition period.

The ^{19}F and ^{1}H NMR spectra were recorded on an Avance III 800 Bruker spectrometer (B_0 = 18.8 T, Larmor frequency = 800.1 MHz for ^{1}H, 752.9 MHz for ^{19}F) using a 1.3 mm ultra-fast MAS probe. The ^{19}F and ^{1}H NMR spectra were recorded at MAS frequency of 60 kHz. The recycle delay was set to 20 s and 30 s for ^{19}F and ^{1}H, respectively. 16 transients were accumulated. The 2D double-quantum single-quantum (DQ–SQ) NMR spectrum was recorded at MAS 62.5 kHz using the $R12_2{}^{5}$[51,52] recoupling pulse sequence. The DQ build-up curves were constructed based on several 2D spectra with recoupling times ranging from 25 to 85 μs. In the 1D NMR experiments, the DEPTH[53] pulse sequence synchronized with the rotor period was applied to suppress existent ^{19}F or ^{1}H background. Phase sensitive detection in the indirect dimension was obtained using the States-TPPI method.[54]

The ^{1}H, ^{13}C, ^{15}N, ^{19}F, ^{67}Zn and ^{27}Al chemical shifts were referenced to proton and carbon signals in TMS, nitromethane, $CFCl_3$, a 1 M solution of $Zn(NO_3)_2$ and a 1 M solution of Al $(NO_3)_3$, respectively. The NMR spectra were reconstructed using the Dmfit[55] software. The CPPI curves were fitted using a home-made routine running in MATLAB.[56] The ^{13}C echo-decay curves were fitted to a mono-exponential decay.

2.5. DFT calculations

All calculations were conducted with the Kohn–Sham[57] density functional theory (DFT) using the CASTEP[58,59] program in the Materials Studio 5.0 environment.[60] For the structure optimization, ultrasoft pseudopotentials were employed, with a plane-wave cut-off energy of 500 eV and a 2 × 2 × 2 Monkhorst–Pack[61] *k*-point sampling grid. During the structure optimization, the cell parameters were kept constant. The Perdew, Burke and Ernzerhof (PBE)[62] functionals were used in the generalized gradient approximation (GGA) for the exchange correlation energy. Magnetic properties were computed using the projector-augmented wave method (GIPAW).[63] For the calculation of the ^{27}Al and ^{67}Zn electric field gradient (EFG) tensor values, a 2 × 2 × 2 Monkhorst–Pack *k*-point grid was used to sample the Brillouin zone, with a plane-wave basis set expanded to kinetics energy lower than 500 eV. For the calculation of the ^{19}F, ^{13}C, ^{15}N and ^{1}H shielding tensor components, a 2 × 2 × 3 Monkhorst–Pack *k*-point grid was used to sample the Brillouin zone, with a plane-wave basis set expanded to kinetics energies lower than 500 eV.

3. Results and discussion

3.1. Thermal analysis

The thermal analysis curves (Fig. 1) show that $Zn_3Al_2F_{12}\cdot[HAmTAZ]_6$ is stable up to 250 °C. The X-ray diffraction pattern of the powder obtained at 800 °C corresponds to a mixture of α-AlF_3 and $ZnCN_2$ (theoretical loss 50.3%, experimental loss 48.3%), which validates the chemical composition proposed.

3.2. SMARTER crystallography

Because all atoms have NMR active nuclei (^{1}H, ^{13}C, ^{15}N, ^{27}Al, ^{67}Zn), $Zn_3Al_2F_{12}\cdot[HAmTAZ]_6$ represents a case study for structure solution by SMARTER crystallography from powder diffraction and solid-state NMR data and quantum mechanical computations.

3.2.1. Determination of the space group and integrant units. The determination of a structural model of such fluorinated hybrid starts with the indexing of the XRPD diagram to extract unit cell parameters and possible space groups. In the case of $Zn_3Al_2F_{12}\cdot[HAmTAZ]_6$, the indexing of the XRPD diagram using the McMaille[64] software indicates a rhombohedral centered hexagonal cell, with refined parameters (Le Bail method):[65] a = 12.583(7) Å and c = 17.649(3) Å. Systematic line extinctions indicate possible space groups $R\bar{3}$, $R32$, $R3m$, $R\bar{3}m$ and $R3$. The second step is to (i) reduce the number of possible space groups; (ii) determine the largest possible part(s) of the integrant unit, including both inorganic framework and organic linkers, to ease the search for an initial structural model. Those stages can be assisted by solid-state NMR.

Cationic framework: ^{27}Al, ^{67}Zn and ^{19}F NMR. The central transition of the ^{27}Al (nuclear spin I = 5/2) MAS NMR spectrum of $Zn_3Al_2F_{12}\cdot[HAmTAZ]_6$ shows a single shapeless resonance (Fig. 2), whose NMR parameters have been determined by reconstruction of the whole spinning sideband pattern: isotropic

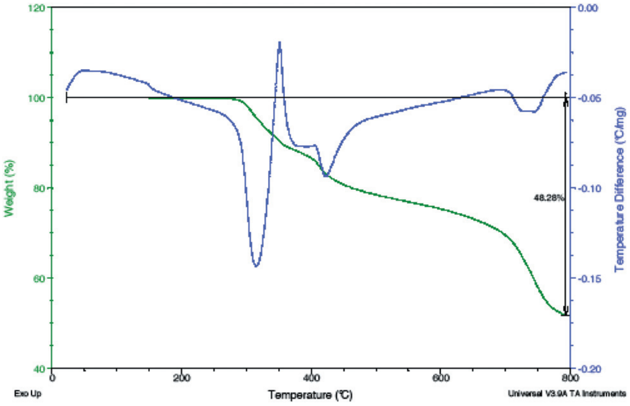

Fig. 1 DTA/TGA curves of $Zn_3Al_2F_{12}\cdot[HAmTAZ]_6$ in the temperature range 25–800 °C.

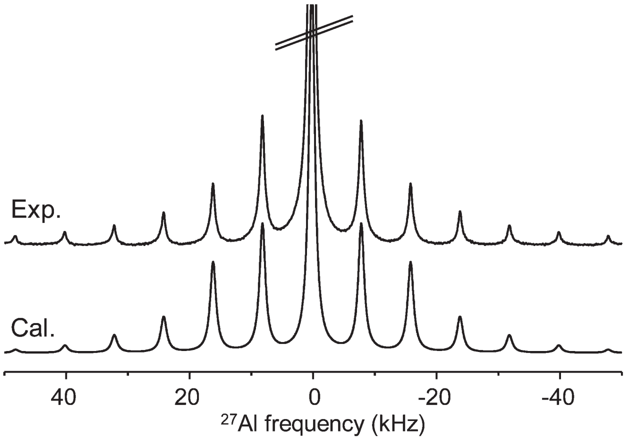

Fig. 2 Experimental and calculated ^{27}Al MAS NMR spectrum of $Zn_3Al_2F_{12}\cdot[HAmTAZ]_6$.

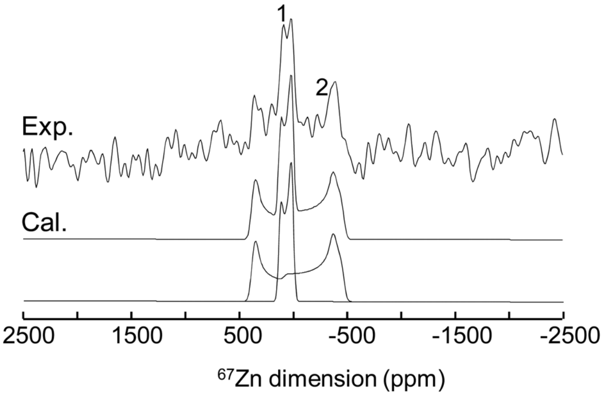

Fig. 3 Experimental and calculated ^{67}Zn static Hahn-echo NMR spectrum of $Zn_3Al_2F_{12}$·[HAmTAZ]$_6$. The two individual contributions are shown below.

Table 1 ^{27}Al and ^{67}Zn line label, line intensity, experimental and calculated from the DFT-optimized structure (in italic) isotropic chemical shift δ_{iso}, quadrupolar coupling constant C_Q and asymmetry parameter η_Q and line assignment in $Zn_3Al_2F_{12}$·[HAmTAZ]$_6$

Line label	Intensity (%)	δ_{iso}/ppm	C_Q/MHz	η_Q	Assignment
^{27}Al					
1	100	1.5 (±0.5)	0.2 (±0.1)	0 (±0.1)	Al1
		1.0	*−0.23*	*0.0*	
^{67}Zn					
1	33 (±1)	83 (±2)	2.9 (±0.1)	0 (±0.1)	Zn1
		72	*2.20*	*0.0*	
2	67 (±1)	87 (±2)	7.5 (±0.1)	0 (±0.1)	Zn2
		82	*6.61*	*0.0*	

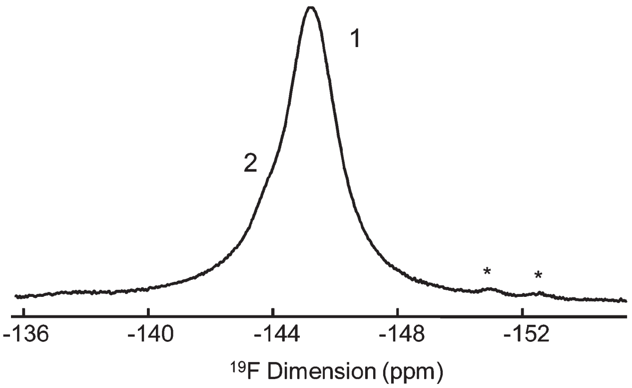

Fig. 4 ^{19}F NMR spectrum of $Zn_3Al_2F_{12}$·[HAmTAZ]$_6$, on which lines are labelled, recorded at ultra-fast MAS (60 kHz) and high-field (18.8 T). Stars indicate non-identified impurities.

chemical shift $\delta_{iso} = -1.5$ ppm, characteristic of an Al atom in six-fold fluorinated coordination, a small quadrupolar coupling constant $C_Q \sim 250$ kHz and the asymmetry parameter $\eta_Q \sim 0$ characteristic of only a slightly distorted AlF_6 octahedron. A single set of parameters has been used for the reconstruction of this NMR spectrum, indicating the absence of distribution of the ^{27}Al quadrupolar parameters and therefore the absence of F/OH substitution in the compound.

^{67}Zn (nuclear spin $I = 7/2$) solid-state NMR is challenging because of the very low sensitivity of this nuclide associated with a large quadrupolar moment[66,67] $Q = 0.15 \times 10^{-28}$ m^2 that broadens the NMR lines. Moreover, the presence of ^{1}H in the structure of $Zn_3Al_2F_{12}$·[HAmTAZ]$_6$ contributes to a strong decrease of the ^{67}Zn non-refocusable transverse relaxation time T_2, making the use of refocusing signal enhancement techniques like Carr–Purcell–Meiboom–Gill (CPMG)[68,69] difficult. Therefore, the ^{67}Zn NMR spectrum of $Zn_3Al_2F_{12}$·[HAmTAZ]$_6$ was recorded at high-field (17.6 T), under static condition using a Hahn-echo pulse sequence. The ^{67}Zn NMR spectrum (Fig. 3) shows two Zn resonances: line 1 at $\delta_{iso} = 83$ ppm, with C_Q = 2.9 MHz and $\eta_Q = 0$, and line 2 at $\delta_{iso} = 87$ ppm, with a larger C_Q = 7.5 MHz and $\eta_Q \sim 0$. The relative intensity of lines 1 and 2 are approximately 1 : 2, respectively (Table 1).

The ^{19}F MAS NMR spectrum of $Zn_3Al_2F_{12}$·[HAmTAZ]$_6$ (Fig. 4), recorded at high-magnetic field (B_0 = 18.8 T) and ultra-fast MAS (62.5 kHz), shows one broad peak with a shoulder on its upper-left part indicating the presence of two inequivalent fluorine sites. Despite the high-resolution conditions employed, the resolution of the two sites is poor, which indicates that the fluorine atoms have very close chemical environments. The ^{19}F isotropic chemical shifts ∼−145 ppm are characteristic of F atoms shared between one aluminum and one zinc atoms.[42] The AlF_6 octahedra are thus isolated from each other.

The ^{19}F, ^{67}Zn and ^{27}Al NMR data indicates that in $Zn_3Al_2F_{12}$·[HAmTAZ]$_6$ the cationic network is built up from AlF_6 octahedra, isolated from each other, but which share fluorine atoms with the Zn polyhedra. By analogy to $ZnAlF_5$·[TAZ],[41] the first coordination shell of the Zn is assumed to be completed by N atoms from the AmTAZ molecules ($ZnF_{6-x}N_x$ octahedra).

Organic linkers: ^{1}H, ^{15}N and ^{13}C NMR. The 1D ^{1}H MAS (62.5 kHz) NMR spectrum of $Zn_3Al_2F_{12}$·[HAmTAZ]$_6$ (Fig. 5a) shows three resonances of relative intensity 24%, 28% and 48%. The line at 7.7 and 6.7 ppm are at positions characteristic of protons attached to a carbon atom and of protons from a NH_2 group, respectively. The ^{1}H resonance at much higher chemical shift (13.8 ppm) indicates that one nitrogen atom of the AmTAZ molecules is protonated, *i.e.* HAmTAZ in the final compound. A 2D ^{1}H–^{1}H NMR spectrum of $Zn_3Al_2F_{12}$·[HAmTAZ]$_6$ (Fig. 5b) was recorded using the symmetry-based homonuclear dipolar recoupling sequence $R12_1^{5}$[5,51,52] a scheme that can be used under ultra-fast MAS conditions. On such a ^{1}H double-quantum single-quantum (DQ–SQ) NMR correlation spectrum, dipolar-coupled inequivalent nuclei will generate a pair of off-diagonal peaks, dipolarly coupled equivalent nuclei will generate a peak on the diagonal, while non-coupled spins will be filtered out by the pulse sequence. The 2D ^{1}H NMR spectrum of $Zn_3Al_2F_{12}$·[HAmTAZ]$_6$ shows intense cross-peaks between the protons from the CH and NH groups, between the protons from the NH_2 and NH groups, between the protons from the CH and NH_2 groups as well as a strong auto-correlation peak for the two protons of the NH_2 group. Diagonal peaks are also present for the NH and CH, which must be due to correlations between two neighbouring amines. This is confirmed by the DQ build-up curves (Fig. 5c) of the two protons from the NH_2 group which present a maximum for a recoupling time ∼65 μs, and decays rapidly afterwards. The auto-correlation peaks for CH and NH

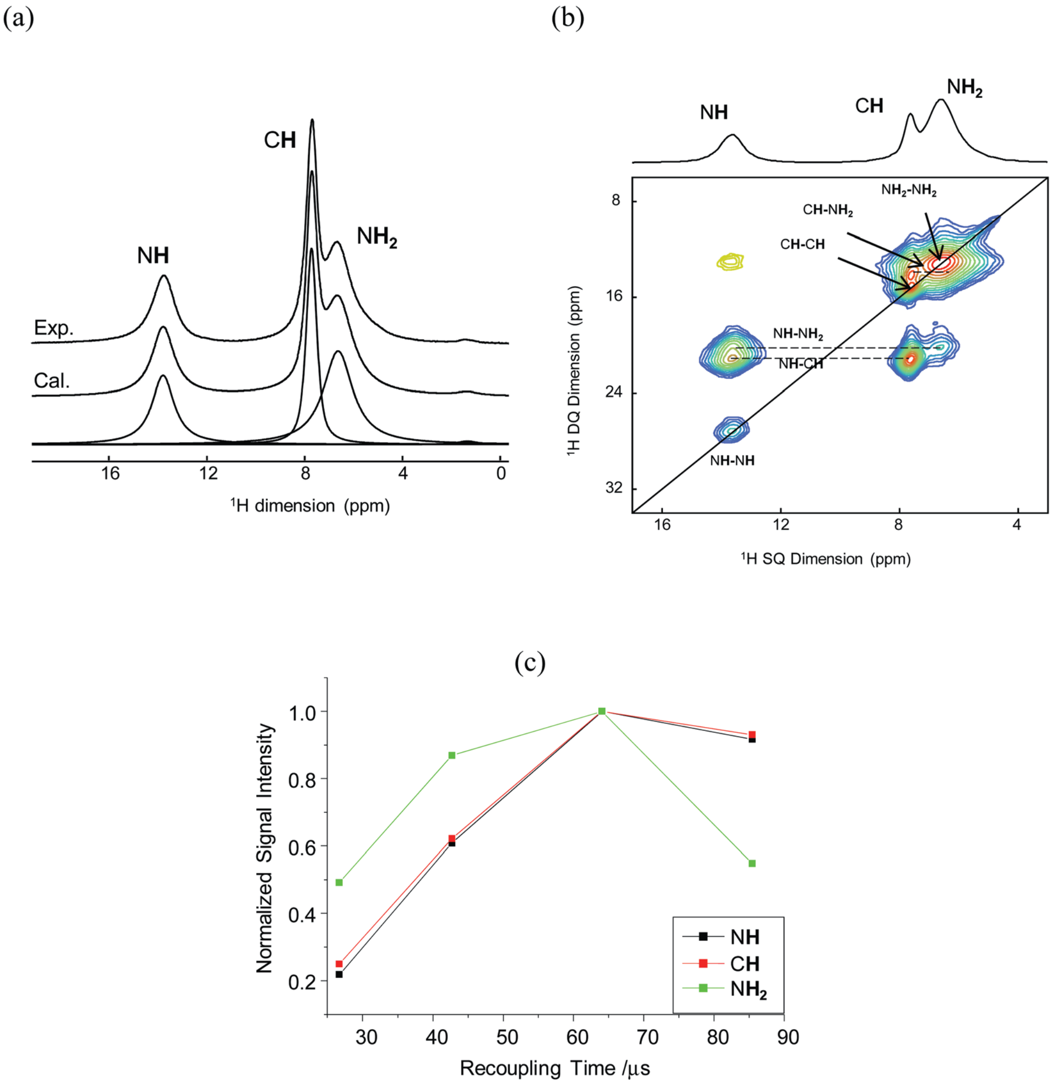

Fig. 5 (a) ^{1}H ultra-fast MAS (62.5 kHz) and high-field (18.8 T) NMR spectrum of $Zn_3Al_2F_{12}\cdot[HAmTAZ]_6$. Lines are assigned. (b) 2D ^{1}H MAS DQ–SQ correlation NMR spectrum. The top spectrum, on which lines are assigned, is the full projection onto the horizontal dimension. Dash lines indicate proton–proton correlations. Thick line is the DQ diagonal (slope of 2). The yellow peak has a negative amplitude. (c) DQ build-up curves for the auto-correlation peaks NH–NH, CH–CH and NH_2–NH_2.

have a slower build up, indicating longer CH–CH and NH–NH distances (as expected between protons from neighboring amines). Finally, one can notice on the 2D DQ–SQ NMR spectrum a peak of negative amplitude with no corresponding peak across the diagonal (Fig. 5b). This peak appears at the δ_{iso} of the NH in the horizontal dimension and at the sum of 2 δ_{iso} of NH_2 in the vertical dimension and therefore it originates from a relayed magnetization transfer from one NH_2 to another NH_2 through the NH.[70]

The ^{15}N CPMAS NMR spectrum of $Zn_3Al_2F_{12}\cdot[HAmTAZ]_6$ (Fig. 6) shows two resonances located at −118 and −163 ppm of relative ratio 1 : 2. The aminotriazole molecule contains four different nitrogen atoms, thus at least four ^{15}N lines were expected on the NMR spectrum of $Zn_3Al_2F_{12}\cdot[HAmTAZ]_6$. Because of the low natural abundance of ^{15}N (below 1%), its low magnetogyric ratio (~1/10 of that of ^{1}H) and usually long

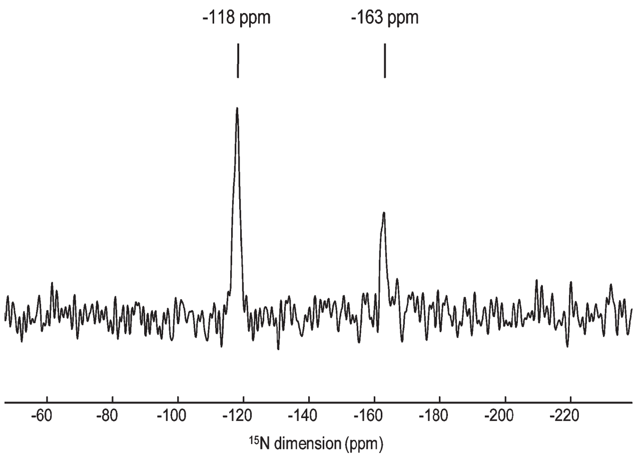

Fig. 6 ^{15}N CPMAS NMR spectrum of $Zn_3Al_2F_{12}\cdot[HAmTAZ]_6$.

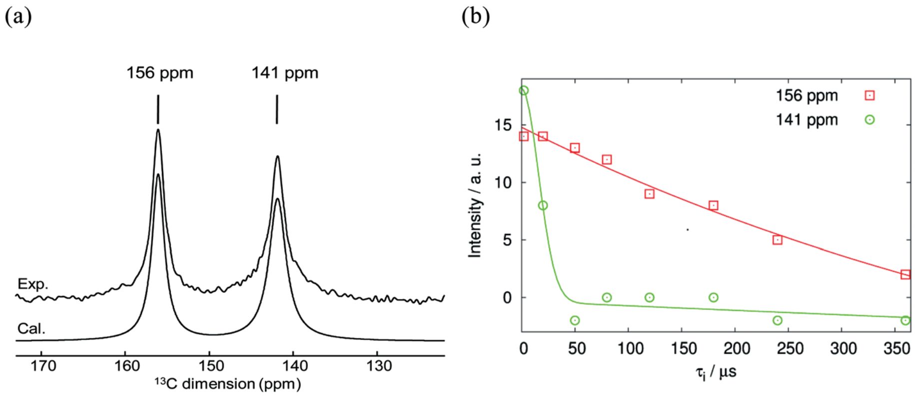

Fig. 7 (a) ^{13}C CPMAS NMR spectrum and (b) CPPI curves of $Zn_3Al_2F_{12}{\cdot}[HAmTAZ]_6$.

Table 2 ^{19}F, ^{1}H, ^{15}N and ^{13}C line label, line intensity, experimental and calculated from the DFT-optimized structure δ_{iso} and line assignment in $Zn_3Al_2F_{12}{\cdot}[HAmTAZ]_6$

Line label	Relative intensity	$\delta_{iso,exp}$ (±1)/ppm	$\delta_{iso,cal}$/ppm	Assignments
^{19}F				
1	1	−144	−146	F2
2	1	−145	−144	F1
^{1}H				
1	1	13.8	15.6	H4
2	1	7.7	8.5	H2
3	2	6.7	7.3 and 8.9	H3a and H3b
^{15}N				
1	2	−118	−115.7	N2
2	1	−163	−161.9	N1
3			−221.3	N4
4			−336.6	N3
^{13}C				
1	1	156	156.3	C2
2	0.9	141	143.9	C1

spin–lattice relaxation times, direct observation of ^{15}N signals is precluded. Therefore, the CPMAS[49] technique, which consists of transferring the magnetization from the surrounding sensitive protons to the nitrogen atoms, has been employed. The augmentation of the ^{15}N spin response is however strongly dependent on the dynamics occurring during the CP transfer, and is usually non-uniform, which may explain why only two of the four expected N signals are observed.

The ^{13}C CPMAS NMR spectrum of $Zn_3Al_2F_{12}{\cdot}[HAmTAZ]_6$ (Fig. 7a) shows two resonances located at δ_{iso} = 141 ppm and 156 ppm (Table 2). In order to identify the nature of the two carbon sites, CPPI experiment was carried out. In such an experiment, the rate of the polarization decay mostly depends on the C–H dipolar interaction. The curve of the line located at 141 ppm (Fig. 7b) decays mono-exponentially, characteristic of a quaternary carbon atom. In contrast, the line at 156 ppm exhibits a bi-exponential decay with turning point for the normalized intensity at zero, characteristic of a carbon atom from a CH group.[71] The relative multiplicity of the two resonances is different from the 1 : 1 ratio expected for the amino-triazole molecule. Quantitativity in CPMAS is difficult to control because of the complex dynamics involved in the CP transfer.[72] In Fig. 8a are shown the CP-build up curves of the two resonances, which represent the intensity of the lines for various CP contact times. The behavior of the two resonances are different and the slower build-up rate for the resonance at 156 ppm confirms its assignment to the quaternary carbon atom of the amine. The strong decay of intensity occurring at longer contact time is due to spin–lattice relaxation of the protons in the rotating frame $T_{1\rho}$. Because of these differences, the ^{13}C CPMAS NMR spectrum of $Zn_3Al_2F_{12}{\cdot}[HAmTAZ]_6$ is not quantitative under the experimental conditions employed in our study. To improve this quantitative aspect of ^{13}C NMR, direct observation of ^{13}C was done. A Hahn-echo sequence was used to remove unwanted signals from the probe, and the inter-pulse delays were synchronized with one rotor period (50 µs). Quantitative measurements in this sequence depends on the transverse relaxation rate T_2 of the nuclei. In the case of $Zn_3Al_2F_{12}{\cdot}[HAmTAZ]_6$, the two ^{13}C resonances have distinct T_2, as shown by the different lines of intensity decay of the two resonances upon increase of the inter-pulse delay (Fig. 8b). Quantitative relative line intensity (close to 1 : 1) was therefore extracted by extrapolating the decay curves to an initial time $t = 0$.

This NMR study indicates that the integrant unit in $Zn_3Al_2F_{12}{\cdot}[HAmTAZ]_6$ is built up from alternating AlF_6 and $ZnF_{6-x}N_x$ octahedra. From these NMR data and the chemical composition, the crystallochemical formula[2,73] of the compound, *i.e.* the chemical formula in which each atom type is split into its inequivalent crystallographic sites, can be derived: $Zn_2Zn_1Al_2F_6F_6[HAmTAZ]_6$. Possible space groups are then those that possess the adequate Wyckoff positions that can embed this crystallochemical formula.[2] In agreement with diffraction data, all hexagonal space groups were automatically tested (see ESI† for the input data of the program: the number and relative ratio of the NMR resonances, the chemical formula, and if known the number of asymmetric units per unit cell). Results indicate that only three of them are compatible with the crystallochemical formula of $Zn_3Al_2F_{12}{\cdot}[HAmTAZ]_6$: $R\bar{3}$, $R32$ and $R\bar{3}m$ (see ESI†). In the $R\bar{3}m$ and $R32$ space groups, all atoms would be in a special position. Since no such special positions are observed on the NMR data, the search for a structural model has been done in the centrosymmetrical space group $R\bar{3}$ (no. 148).

3.2.2. Structural model. Once a space group is selected and part of the IU defined, an initial structural model has to be

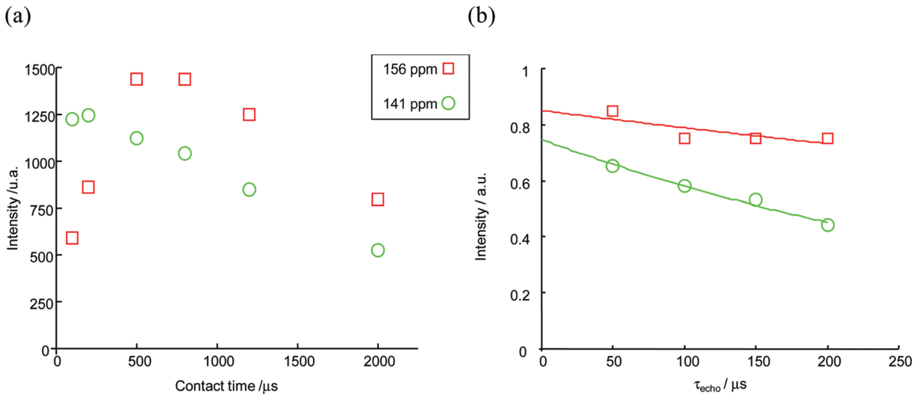

Fig. 8 ^{13}C (a) CP build-up curves and (b) Hahn-echo decay curves for the two ^{13}C resonances in $Zn_3Al_2F_{12}{\cdot}[HAmTAZ]_6$.

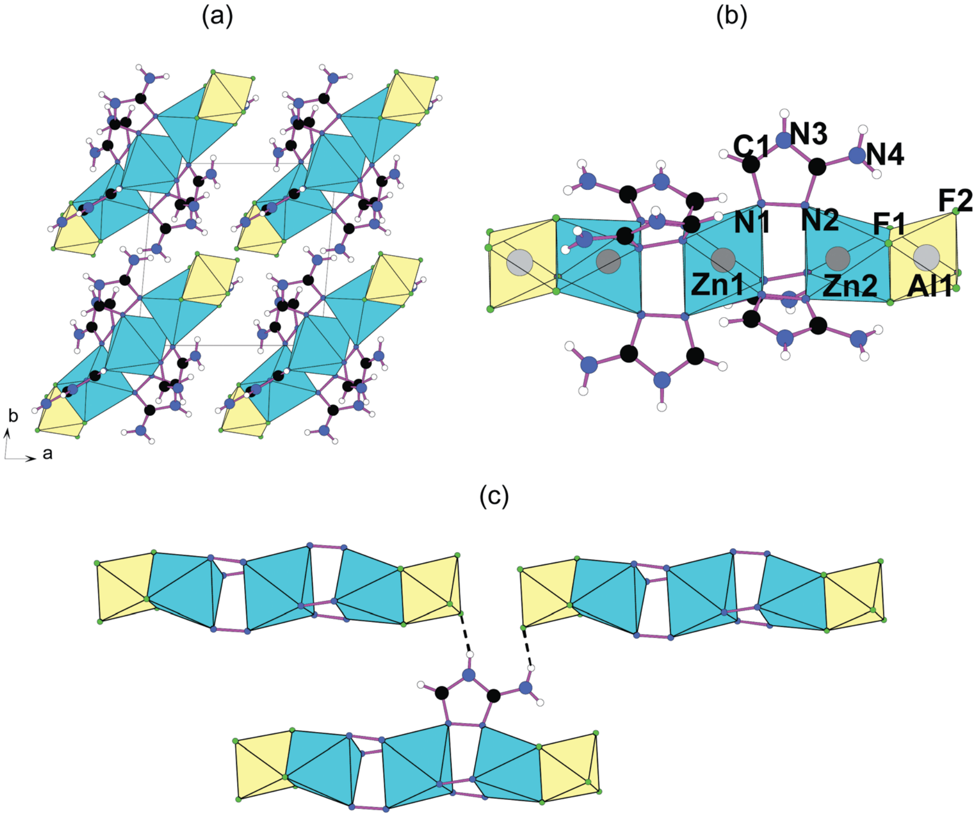

Fig. 9 (a) Projection of the structure of $Zn_3Al_2F_{12}{\cdot}[HAmTAZ]_6$ in the rhombohedric unit cell along the [001] axis. (b) Representation of a cluster showing the environments of the Al^{3+} and Zn^{2+} cations. (c) Representation of the environment of an amine: N1 and N2 are bonded to the Zn1 and Zn2 atoms by iono-covalent bonds. N3 and N4 form hydrogen bonds (dash lines) with two fluorine atoms from a neighboring cluster. For the sake of clarity, only one amine is shown.

found. This can be done, for example, by using Monte Carlo-based software like FOX[74,75] or Espoir.[76] Partial or complete knowledge of the IU at this stage is of great importance since it reduces the number of independent atomic coordinates to be determined. According to the NMR experiments, the input data in the software FOX for $Zn_3Al_2F_{12}{\cdot}[HAmTAZ]_6$ are an AmTAZ molecule, an AlF_6 octahedron and 2 independent Zn atoms. The search, carried out using the XRPD as cost function, converged to a structural model, which was then refined by the Rietveld method from the powder diffraction data (R_p = 10.3%, R_{wp} = 12.2%, R_{Bragg} = 5.63%, see ESI†).

The structure of $Zn_3Al_2F_{12}{\cdot}[HAmTAZ]_6$ is built up from isolated clusters (Fig. 9). Each cluster contains two crystallographically inequivalent Zn atoms and one six-fold fluorinated coordinated aluminium atom. Zn(1) is surrounded by six amines ($d_{Zn(1)–N}$ = 2.18 Å), half of them being also connected to Zn(2) ($d_{Zn(2)–N}$ = 2.03 Å). Three fluorine atoms complete the coordination sphere of Zn(2). The Al and Zn polyhedra share a face.

Because the Zn(1) ion sits on a −3 symmetry axis, the ZnN_6 octahedron is regular with all six Zn–N distances equal to 2.18 Å. On the contrary, the ZnN_3F_3 is much more distorted, with Zn(2)–N distances (2.03 Å) shorter than the Zn(2)–F distances (2.17 Å). Similarly, in the AlF_6 octahedron, the Al–$F_{bridging}$ distances (1.84 Å) are longer than the Al–$F_{non\text{-}bridging}$ distances (1.77 Å). The amines are bonded to two Zn ions through iono-covalent bonds and also form strong hydrogen bonds (average N–F distance of 2.70 Å) with the F atoms from two neighbouring clusters, yielding a three-dimensional character to the solid network.

3.3. Structure validation and optimization: DFT calculation of NMR parameters

Validation of a structural model can be done by comparing NMR parameters (shielding, electric field gradient tensors) determined experimentally with parameters calculated *ab initio* from the structural model. In inorganic fluorides, geometry optimization is often required to improve the agreement between experimental and calculated parameters,[14,15,42,77,78] mostly because the positions of the light F and H atoms can be difficult to determine from X-ray diffraction data only (powder or single-crystal). Optimization of the structure of $Zn_3Al_2F_{12}\cdot[HAmTAZ]_6$ was done using DFT-based code CASTEP package,[58,59] keeping the cell parameters unchanged. The optimized atomic coordinates are given in Table 3. Single crystals of $Zn_3Al_2F_{12}\cdot[HAmTAZ]_6$ were also obtained. An independent structure solution could thus be obtained from single crystal X-ray diffraction measurements (Table 3). The structure model extracted from SMARTER crystallography of the polycrystalline powder of $Zn_3Al_2F_{12}\cdot[HAmTAZ]_6$ is close to the single-crystal model (atomic fractional coordinate differences below 0.06, see Table 3 and ESI†).

Table 3 Atom labels, Wyckoff positions, atomic coordinates (*x*,*y*,*z*) of the DFT-optimized structure and of the structure of $Zn_3Al_2F_{12}\cdot[HAmTAZ]_6$ determined from single-crystal diffraction data (in italic). Only the DFT-optimized positions are given for the protons. Uncertainties are given in brackets

Atom	Wyckoff	*x*	*y*	*Z*
Zn1	1a	0	0	0
		0	*0*	*0*
Zn2	2c	0	0	0.2030
		0	*0*	*0.2055(2)*
Al1	2c	0	0	0.3634
		0	*0*	*0.36462(5)*
F1	6f	0.04717	0.1925	0.4197
		0.0854(1)	*0.1356(1)*	*0.41860(6)*
F2	6f	0.1853	0.0683	0.2834
		0.1290(1)	*0.0479(1)*	*0.29831(6)*
N1	6f	0.1138	0.1592	0.1488
		0.1117(2)	*0.1575(1)*	*0.1484(1)*
N2	6f	0.0967	0.1645	0.0705
		0.0981(2)	*0.1638(2)*	*0.0702(1)*
C1	6f	0.1641	0.2742	0.0505
		0.1628(2)	*0.2788(2)*	*0.0520(1)*
C2	6f	0.1928	0.2817	0.1726
		0.1860(2)	*0.2708(2)*	*0.1723(1)*
H2	6f	0.1708	0.3186	0.9936
N3	6f	0.2260	0.3533	0.1117
		0.2187(2)	*0.3484(2)*	*0.1132(1)*
H3a	6f	0.1925	0.2372	0.2834
H3b	6f	0.2574	0.3942	0.2606
N4	6f	0.2380	0.3069	0.2444
		0.2263(2)	*0.3027(2)*	*0.2441(1)*
H4	6f	0.2894	0.4509	0.1090

The NMR parameters (^{27}Al and ^{67}Zn EFGs, ^{1}H, ^{13}C, ^{15}N, ^{19}F δ_{iso}) were calculated from the optimized structure (Tables 1 and 2). They agree rather well with the experimental values, which validates the proposed structural model. The low ^{27}Al quadrupolar coupling constant C_Q as well as the difference in C_Qs between the two Zn atoms determined experimentally are well reproduced by the calculations. The ^{19}F δ_{iso} values calculated for the two F sites are very close to each other (difference below 1 ppm), explaining why they were not resolved on the ^{19}F MAS NMR spectrum (Fig. 4), despite the high-magnetic field and ultra-fast MAS conditions employed. Because the closeness in δ_{iso} stands within the accuracy of the DFT calculations, the proposed line assignment is not completely certain. The calculated ^{15}N δ_{iso} values (Table 2) shows that the two lines observed on the ^{15}N CP-MAS NMR spectrum (Fig. 6) arise from the nitrogen atoms N(1) and N(2) linked to the Zn atoms. The calculated ^{13}C δ_{iso} (Table 2) are close to the experimental values and confirm the line assignment deduced from the ^{13}C CPPI experiment (Fig. 7b). Finally, the calculated chemical shifts of the protons (Table 2) are close to the experimental values, which indicates that the protons have been well positioned during the geometry optimization. The good agreement between six independent sets of experimental and calculated NMR parameters, one for each type of nucleus in the compound (^{27}Al, ^{67}Zn, ^{19}F, ^{15}N, ^{13}C and ^{1}H), is a strong support for the reliability of the optimized model of $Zn_3Al_2F_{12}\cdot[HAmTAZ]_6$, including the positions of the protons, which could not be obtain from diffraction data (even from single-crystal).

4. Conclusions

SMARTER crystallography structure resolution of the fluorinated hybrid sample $Zn_3Al_2F_{12}\cdot[HAmTAZ]_6$ has been presented. Combination of powder X-ray diffraction, solid-state NMR data and quantum computation (structure optimization and NMR parameter calculations) have yielded an accurate structural model for $Zn_3Al_2F_{12}\cdot[HAmTAZ]_6$. This class of samples is of particular interest since all the atoms have NMR accessible isotopes. In $Zn_3Al_2F_{12}\cdot[HAmTAZ]_6$, ^{27}Al and high-field ^{19}F and ^{67}Zn NMR give access to the inorganic part of the framework while ^{1}H, ^{13}C and ^{15}N NMR yield insights into the organic linkers. From these experiments, parts of the integrant unit have been determined and taken as input data for the search of a structural model from the powder diffraction data. The optimization of the atomic positions and the calculations of NMR parameters (^{27}Al and ^{67}Zn quadrupolar parameters and ^{19}F, ^{1}H, ^{13}C and ^{15}N isotropic chemical shifts) has been done using DFT code. In this methodological approach, validation has also been obtained for $Zn_3Al_2F_{12}\cdot[HAmTAZ]_6$ with the structural model obtained independently from single-crystal diffraction data, as well as with the good agreement between six independent sets of experimental and calculated NMR parameters. Through the example of $Zn_3Al_2F_{12}\cdot[HAmTAZ]_6$, we have shown that by SMARTER crystallography, structural models could be obtained from powder X-ray diffraction data with NMR and modelling, with a quality similar to that obtained from single-crystal diffraction measurements. This approach also allows us to go even further by providing the localization of the protons.

Acknowledgements

Financial support from the TGE RMN THC FR3050 for conducting the research is gratefully acknowledged. CM thanks Dr Franck Fayon (CEMHTI Orléans, France) and Dr Julien Trébosc (UCCS Lille, France) for their help in the high-field NMR measurements. AC and KA thank Prof. Marc Leblanc (IMMM Le Mans, France) for helpful discussions.

References

1 A. Le Bail, L. M. D. Cranswick, K. Adil, A. Altomare, M. Avdeev, R. Cerny, C. Cuocci, C. Giacovazzo, I. Halasz, S. H. Lapidus, J. N. Louwen, A. Moliterni, L. Palatinus, R. Rizzi, E. C. Schilder, P. W. Stephens, K. H. Stone and J. van Mechelen, *Powder Diffr.*, 2009, **24**, 254.

2 F. Taulelle, Fundamental Principles of NMR Crystallography, in *NMR Crystallography*, ed. R. K. Harris, R. Wasylishen and M. Duer, J. Wiley & Sons Ltd, Chichester UK, 2009, p. 245.

3 J. Senker and J. Lüdecke, *Z. Naturforsch.*, 2001, **56b**, 1089.

4 J. Senker, L. Seyfarth and J. Voll, *Solid State Sci.*, 2004, **6**, 1039.

5 L. Seyfarth, J. Sehnert, N. E. A. El-Gamel, W. Milius, E. Kroke, J. Breu and J. Senker, *J. Mol. Struct.*, 2008, **889**, 217.

6 R. K. Harris, in *NMR Crystallography*, ed. R. K. Harris, R. D. Wasylishen and M. J. Duer, John Wiley & Sons Ltd, Chichester, 2009, ch. 1, p. 1.

7 R. K. Harris, P. Hodgkinson, V. Zorin, J.-N. Dumez, B. Elena-Herrmann, L. Emsley, E. Salager and R. S. Stein, *Magn. Reson. Chem.*, 2010, **48**, S103.

8 X. Filip, G. Borodi and C. Filip, *Phys. Chem. Chem. Phys.*, 2011, **13**, 17978–17986.

9 L. Seyfarth, J. Seyfarth, B. V. Lotsch, W. Schnick and J. Senker, *Phys. Chem. Chem. Phys.*, 2010, **12**, 2227.

10 L. Seyfarth and J. Senker, *Phys. Chem. Chem. Phys.*, 2009, **11**, 3522.

11 J. Dutour, N. Guillou, C. Huguenard, F. Taulelle, C. Mellot-Draznieks and G. Férey, *Solid State Sci.*, 2004, **6**, 1059.

12 M. Body, G. Silly, C. Legein, J.-Y. Buzaré, F. Calvayrac and P. Blaha, *J. Solid State Chem.*, 2005, **178**, 3655.

13 C. Martineau, F. Fayon, C. Legein, J.-Y. Buzaré, F. Goutenoire and E. Suard, *Inorg. Chem.*, 2008, **47**, 10895.

14 C. Martineau, F. Fayon, C. Legein, J.-Y. Buzaré, M. Body, D. Massiot and F. Goutenoire, *Dalton Trans.*, 2008, 6150.

15 C. Martineau, F. Fayon, M. R. Suchomel, M. Allix, D. Massiot and F. Taulelle, *Inorg. Chem.*, 2011, **50**, 2644.

16 H. Gies and B. Marler, *Zeolites*, 1992, **12**, 42.

17 D. H. Brouwer, *J. Am. Chem. Soc.*, 2008, **130**, 6306.

18 D. H. Brouwer, *J. Magn. Reson.*, 2008, **194**, 136.

19 D. H. Brouwer, R. J. Darton, R. E. Morris and M. H. Levitt, *J. Am. Chem. Soc.*, 2005, **127**, 10365.

20 S. Cadars, D. H. Brouwer and B. F. Chmelka, *Phys. Chem. Chem. Phys.*, 2009, **11**, 1825.

21 D. H. Brouwer, I. L. Moudrakovski, R. J. Darton and R. E. Morris, *Magn. Reson. Chem.*, 2010, **48**, S113.

22 L. Beitone, C. Huguenard, A. Gansmüller, M. Henry, F. Taulelle, T. Loiseau and G. Férey, *J. Am. Chem. Soc.*, 2003, **125**, 9102.

23 L. Beitone, J. Marrot, T. Loiseau, G. Férey, M. Henry, C. Huguenard, A. Gansmüller and F. Taulelle, *J. Am. Chem. Soc.*, 2003, **125**, 1912.

24 T. Ahnfeldt, N. Guillou, D. Gunzelmann, I. Margiolaki, T. Loiseau, G. Férey, J. Senker and N. Stock, *Angew. Chem., Int. Ed.*, 2009, **48**, 5163.

25 M. Haouas, C. Volkringer, T. Loiseau, G. Férey and F. Taulelle, *Chem.–Eur. J.*, 2009, **15**, 3139.

26 T. Ahnfeldt, D. Gunzelmann, T. Loiseau, D. Hirsemann, J. Senker, G. Férey and N. Stock, *Inorg. Chem.*, 2009, **48**, 3057.

27 J. Y. Jiang, J. Huang, S. Marx, W. Kleist, M. Hunger and A. Baiker, *J. Phys. Chem. Lett.*, 2010, **1**, 2886.

28 R. Hajjar, C. Volkringer, T. Loiseau, N. Guillou, J. Marrot, G. Férey, I. Margiolaki, G. Fink, C. Morais and F. Taulelle, *Chem. Mater.*, 2011, **23**, 39.

29 J. P. S. Mowat, S. R. Miller, A. M. Z. Slawin, V. R. Seymour, S. E. Ashbrook and P. A. Wright, *Microporous Mesoporous Mater.*, 2011, **142**, 322.

30 C. Yang, X. Wang and M. A. Omary, *J. Am. Chem. Soc.*, 2007, **129**, 15454.

31 C. A. Fernandez, R. K. Thallapally, R. K. Motkuri, S. K. Nune, J. C. Sumrak, J. Tian and J. Liu, *Cryst. Growth Des.*, 2010, **10**, 1037.

32 T. Devic, P. Horcajada, C. Serre, F. Salles, G. Maurin, B. Moulin, D. Heurtaux, G. Clet, A. Vimont, J.-M. Grenèche, B. Le Ouay, F. Moreau, E. Magnier, Y. Filinchuk, J. Marrot, J.-C. Lavalley, M. Daturi and G. Férey, *J. Am. Chem. Soc.*, 2010, **132**, 1127.

33 P. Horcajada, F. Salles, S. Wuttke, T. Devic, D. Heurtaux, G. Maurin, A. Vimont, M. Daturi, O. David, E. Magnier, N. Stock, Y. Filinchuk, D. Popov, C. Riekel, G. Férey and C. Serre, *J. Am. Chem. Soc.*, 2011, **133**, 17839.

34 P. Pachfule, Y. Chen, J. Jian and R. Banerjy, *Chem.–Eur. J.*, 2012, **18**, 688.

35 C. Yang, X. Wang and M. A. Omary, *J. Am. Chem. Soc.*, 2007, **129**, 15454.

36 C. A. Fernandez, R. K. Thallapally, R. K. Motkuri, S. K. Nune, J. C. Sumrak, J. Tian and J. Liu, *Cryst. Growth Des.*, 2010, **10**, 1037.

37 Z. Hulvey, D. A. Sava, J. Eckert and A. K. Cheetham, *Inorg. Chem.*, 2011, **50**, 403.

38 C. Yang, U. Kaipa, Q. Z. Mather, X. Wang, V. Nesterov, A. F. Venero and M. A. Omary, *J. Am. Chem. Soc.*, 2011, **133**, 18094.

39 M. A. Goforth, C.-Y. Su, R. Hipp, R. B. Macquart, M. D. Smith and H.-C. Loye, *J. Solid State Chem.*, 2005, **178**, 2511.

40 D. L. Rogow, G. Zapeda, C. H. Swanson, X. Fan, C. F. Campana, A. G. Oliver and S. R. J. Oliver, *Chem. Mater.*, 2007, **19**, 4658.

41 L. Liu, X. Wang and A. J. Jacobsen, *Dalton Trans.*, 2010, **39**, 1722.

42 A. Cadiau, C. Martineau, M. Leblanc, V. Maisonneuve, A. Hémon-Ribaud, F. Taulelle and K. Adil, *J. Mater. Chem.*, 2011, **21**, 3949.

43 H. M. Rietveld, *J. Appl. Crystallogr.*, 1969, **2**, 65.

44 J. R. Carjaval, *FULLPROF Program, Rietveld Pattern Matching Analysis of Powder Patterns*, ILL, Grenoble, 1990.

45 G. M. Sheldrick, *Appl. Crystallogr.*, 2008, **A64**, 112.

46 L. J. J. Farrugia, *J. Appl. Crystallogr.*, 1999, **32**, 837.

47 B. M. Fung, A. K. Khitrin and K. Ermolaev, *J. Magn. Reson.*, 2000, **142**, 97.

48 X. Wu and K. W. Zilm, *J. Magn. Reson., Ser. A*, 1993, **102**, 205.

49 J. Schaefer and E. O. Stejskal, *J. Am. Chem. Soc.*, 1976, **89**, 1031.

50 S. R. Hartmann and E. L. Hahn, *Phys. Rev.*, 1962, **128**, 2042.

51 M. Carravetta, M. Eden, X. Zhao, A. Brinkmann and M. H. Levitt, *Chem. Phys. Lett.*, 2000, **321**, 205.

52 L. Mafra, R. Siegel, C. Fernandez, D. Schneider, F. Aussenac and J. Rocha, *J. Magn. Reson.*, 2009, **199**, 111.

53 D. G. Cory and W. M. Ritchey, *J. Magn. Reson.*, 1988, **80**, 128.

54 D. Marion, M. Ikura, R. Tschudin and A. Bax, *J. Magn. Reson.*, 1989, **85**, 393.

55 D. Massiot, F. Fayon, M. Capron, I. King, S. Le Calvé, B. Alonso, J. O. Durand, B. Bujoli, Z. Gan and G. Hoatson, *Magn. Reson. Chem.*, 2002, **40**, 70.

56 The language of technical computing: MATLAB; Maths Works Inc., 24 Prime Park Way, Natick, MA 01760-150, Copyright 1984–2004.

57 W. Kohn and L. Sham, *Phys. Rev.*, 1965, **140**, 1133.

58 M. D. Segall, P. L. D. Lindan, M. J. Probert, C. J. Pickard, P. J. Hasnip, S. J. Clark and M. C. Payne, *J. Phys.: Condens. Matter*, 2002, **14**, 2717.

59 S. J. Clark, M. D. Segall, C. J. Pickard, P. J. Hasnip, M. J. Probert, K. Refson and M. C. Payne, *Z. Kristallogr.*, 2005, **220**, 567.

60 http://accelrys.com

61 H. J. Monkhorst and J. D. Pack, *Phys. Rev. B: Solid State*, 1976, **13**, 5188.

62 J. P. Perdew, K. Burke and M. Ernzerhof, *Phys. Rev. Lett.*, 1996, **77**, 3865.

63 C. J. Pickard and F. Mauri, *Phys. Rev. B: Condens. Matter*, 2001, **63**, 245101.

64 A. Le Bail, *Powder Diffr.*, 2004, **19**, 249.

65 A. Le Bail, H. Duroy and J. L. Fourquet, *Mater. Res. Bull.*, 1988, **23**, 447.

66 P. Pyykkö, *Mol. Phys.*, 2001, **99**, 1617.

67 P. Pyykkö, *Mol. Phys.*, 2008, **106**, 1965.
68 T. Vosegaard, F. H. Larsen, H. J. Jakobsen, P. D. Ellis and N. C. Nielsen, *J. Am. Chem. Soc.*, 1997, **119**, 9055.
69 F. H. Larsen, H. J. Jakobsen, P. D. Ellis and N. C. Nielsen, *J. Magn. Reson.*, 1998, **131**, 144.
70 R. R. Ernst, G. Bodenhausen and A. Wokaun, *Principles of Nuclear Magnetic Resonance in One and Two Dimensions*, Oxford University Press, Oxford, UK, 1994.
71 C. Gervais, F. Babonneau, J. Maquet, C. Bonhomme, D. Massiot, E. Framery and M. Vaultier, *Magn. Reson. Chem.*, 1998, **36**, 407.
72 S. Ding, C. A. McDowell and C. Ye, *J. Magn. Reson., Ser. A*, 1994, **109**, 6.
73 F. Taulelle, *Solid State Sci.*, 2004, **6**, 1053.
74 V. Favre-Nicolin and R. Cerny, *J. Appl. Crystallogr.*, 2002, **35**, 734.
75 http://objcryst.sourceforge.net
76 A. Le Bail, *Powder Diffr.*, 2005, **20**, 316.
77 M. Body, G. Silly, C. Legein, J.-Y. Buzaré, F. Calvayrac and P. Blaha, *J. Solid State Chem.*, 2005, **178**, 3655.
78 A. Zheng, S.-B. Liu and F. Deng, *J. Phys. Chem. C*, 2009, **113**, 15018.